Atmospheric Environment 229 (2020) 117431

Contents lists available at ScienceDirect

Atmospheric Environment

journal homepage: www.elsevier.com/locate/atmosenv

A new anisotropic adaptive mesh photochemical model for ozone formation in power plant plumes

J. Zheng [a], F. Fang [b,*], Z. Wang [c], J. Zhu [d], J. Li [c], J. Li [d], H. Xiao [a], C.C. Pain [b]

[a] Center for Excellence in Regional Atmospheric Environment, Institute of Urban Environment, Chinese Academy of Sciences, Xiamen, 361021, China
[b] Department of Earth Science and Engineering, Imperial College London, United Kingdom of Great Britain and Northern Ireland
[c] State Key Laboratory of Atmospheric Boundary Layer Physics and Atmospheric Chemistry, Institute of Atmospheric Physics, Chinese Academy of Sciences, Beijing 100029, China
[d] International Center for Climate and Environment Sciences, Institute of Atmospheric Physics, Chinese Academy of Sciences, Beijing 100029, China

ARTICLE INFO

Keywords:
Adaptive meshes
PinG
Ozone
Plume
Photochemical model
CBM-Z
Fluidity-Chem

ABSTRACT

In this work, an advanced dynamically adaptive unstructured mesh technique is introduced to photochemical modeling, which provides a consistent way to resolve the complex chemical transport processes over a wide range of spatial scales from meters (near point sources) up to hundred kilometers without the Gaussian distribution assumption (often used in existing subgrid Plume-in-Grid (PinG) models, such as RPM and SCICHEM). To assess the performance of the new photochemical model, the numerical results (NO_x and O_3) have been compared to the Southern Oxidants Study (SOS) 1999 aircraft plume measurements, where the range of the emission intensity is from 1.8 to 13.9 ton/h. The relative error in the peak value of NO_x and O_3 is between 10%–20% within 66 km downwind distance. The results show that the use of dynamically adaptive meshes can reproduce the details of the plume chemistry evolution: the slender puff structure of high NO_x concentrations within a few kilometers width near the point sources, and the wing-like structure of ozone concentration during the plume growth, which is hard to capture for the PinG models or photochemical grid models.

1. Introduction

Air quality modeling systems mainly involve three components: emissions, meteorology and chemical transport. Once air pollutants are emitted into the atmosphere, the dynamic and chemical processes would transport and transform them continuously (Garcia-Menendez and Odman, 2011; Kühnlein, 2011). The interactions between these processes involve a wide range of spatial scales. The initial transformation of emissions from urban and industrial centers or dispersion of plumes from large power plant stacks occurs on relatively small scales, but would be engaged to much larger scales after long distance transport (Zheng et al., 2015; Kühnlein, 2011; Behrens, 2006). In air quality modeling it is challenging to accurately represent the nonlinear photochemical processes from a very fine scale (a few meters, near point sources) to a large scale (several kilometers up to 100 km) simultaneously (Karamchandani et al., 2011).

The large scale grid models are unable to catch the sharp change in pollutant concentrations, thus leading to an artificial dilution of stack emissions and incorrect chemical reaction rates (Taghavi et al., 2004; Arunachalam et al., 2006; Queen and Zhang, 2008). It is known that the NO_x plume evolution near point sources is dominated by high NO_x concentrations, thus the ozone formation is suppressed (Ryerson et al., 2001, 1998). However the artificial dilution of the NO_x emissions in the grid models results in a short lifetime of NO_x (Kim et al., 2017; Chowdhury et al., 2015). To overcome this issue, most of existing air quality models (e.g., CMAQ, CAMx, and WRF-Chem) have incorporated subgrid-scale Plume-in-Grid (PinG) modules (Karamchandani et al., 2011, 2000; Mauzerall et al., 2005; Karamchandani et al., 2012). In contrast to the traditional Eulerian method, the PinG technique uses the Lagrangian approach to simulate the plume dynamic and chemical processes (plume initialization, growth and mature stages) at the small spatial and temporal scales. The results from the PinG modules are then integrated into the large scale grid models. The PinG modules can be used for eliminating some error associated with grid models, thus improving the accuracy of ozone concentrations at the plume initialization stage. However, they suffer from the limitations in representation of physical phenomena (e.g., the effect of wind shear), complex dispersion processes and interaction of plumes between point sources (Chowdhury et al., 2015; Karamchandani et al., 2011). In existing photochemical sub-grid scale models (including PinG), it is still

* Corresponding author.
E-mail address: f.fang@imperial.ac.uk (F. Fang).

https://doi.org/10.1016/j.atmosenv.2020.117431
Received 19 August 2019; Received in revised form 17 March 2020; Accepted 21 March 2020
Available online 31 March 2020

challenging to capture the wing-like structures of ozone concentration (occurred at the plume growth stage) over a long distance, especially for large plume emissions (Chowdhury et al., 2015).

Over embedded sub-grid scale PinG modeling and static nested grid techniques, adaptive mesh modeling may be the best approach to resolve multiscale dynamic and chemical processes in a consistent way (Garcia-Menendez and Odman, 2011; Zheng et al., 2015; Kühnlein, 2011; Behrens, 2006; Weller et al., 2010; Nikiforakis, 2009; Piggott et al., 2009). In dynamic mesh adaptations, mesh resolution can be changed automatically to improve the accuracy of model results, to capture detailed dynamics or follow the chemical evolution of plumes (Garcia-Menendez et al., 2010). The adaptive grid approach was introduced to atmospheric modeling (Dietachmayer and Droegemeier, 1992) and an air quality model for an ozone episode by Odman et al. (2004), Odman and Khan (2002). The dynamic mesh adaption technique used in their work is mesh movement (i.e. r-adaptivity) where the nodes are optimally relocated to resolve the small-scale features of interest. The total number of nodes is fixed in r-adaptivity (Srivastava et al., 2000; Lagzi et al., 2009; Kühnlein et al., 2012; Nikiforakis, 2009). Another widely used adaptive mesh technique is adaptive mesh refinement (AMR) (also called h-adaptivity) where the mesh is refined locally by adding grid points when/where it is needed (Baker et al., 2013; Constantinescu et al., 2008; Piggott et al., 2005). The combination of h- and r-adaptive method is called hr-adaptivity where the mesh is optimally relocated and refined/coarsen to allow for maximum flexibility in adapting to solution features. More recently, an anisotropic hr-adaptive mesh technique has been introduced into air quality transport (advection) modeling (Zheng et al., 2015) which has been successfully applied to the simulation of about 100 power plant plumes over the whole Shanxi-Hebei-Shandong-Henan region of China with a 1090 km × 1060 km domain.

In this work, an anisotropic adaptive mesh photochemical model (Fluidity-Chem) has been developed by integrating the widely used Carbon Bond Mechanism Z (CBM-Z) (Zaveri and Peters, 1999) with the newly developed adaptive unstructured mesh air quality model (Zheng et al., 2015; Pain et al., 2005; Piggott et al., 2009, 2008a,b). This work provides a single unified integrated model for resolving chemical reaction and transport processes over a wide range of spatial scales from microscale (hundred meters) to regional scale (hundred kilometers). The capability of Fluidity-Chem has been demonstrated by solving the plume emitted from power plants. A comparison between the numerical results and SOS 1999 aircraft plume data has been carried out.

The sections of this article are set out as follows. In Section 2, the governing equation for atmospheric chemical transport modeling and its numerical discretization are introduced. In Section 3, the photochemical mechanism is first described briefly, followed by introducing an unstructured mesh fluid model (Fluidity) along with the details of the dynamically adaptive mesh technique. The integration of Fluidity and CBM-Z is finally given in Section 3.3. Section 4 demonstrates the capability of Fluidity-Chem in numerical test cases and provides the comparison between the computed and observed results and the corresponding discussion. The summary and conclusions are presented in Section 5.

2. Multi-pollutant chemical transport models and its discretization

In air quality modeling, we consider the generic atmospheric chemical transport equation in a conservative form:

$$\frac{\partial c_k}{\partial t} + \nabla\cdot(\boldsymbol{u}c_k) - \nabla\cdot(\bar{\bar{\kappa}}\nabla c_k) = S_k + R_k(c_1,\dots,c_K),\ k\in\{1,\dots,\mathcal{K}\}, \tag{1}$$

where c_k is the mass concentration of chemical species k, $\mathcal{K}$ is the number of species, $\boldsymbol{u} = (u,v,w)^{\mathrm{T}}$ is the velocity vector, $\bar{\bar{\kappa}}$ is the turbulent diffusivity (tensor), S_k is the source term of species k, and R_k represents the net generation of species k by chemical reactions, which is the coupled term between the flow (Fluidity) and chemical (CBM-Z) dynamics. Eq. (1) can be split into two stages during each time step $[n, n+1]$: first, the advection and diffusion are considered,

$$\frac{c_k^{n+1,*} - c_k^n}{\Delta t} + \nabla\cdot(\boldsymbol{u}c_k) - \nabla\cdot(\bar{\bar{\kappa}}\nabla c_k) = S_k,\ k\in\{1,\dots,\mathcal{K}\}, \tag{2}$$

where Δt is the time step; second, the chemical reactions between species are solved (for details, see Section 3.1):

$$\frac{c_k^{n+1} - c_k^{n+1,*}}{\Delta t} = R_k(c_1,\dots,c_K),\ k\in\{1,\dots,\mathcal{K}\}, \tag{3}$$

Integrating equation (2) by parts over the computational domain Ω, its weak form can be written as:

$$\begin{aligned}&\int_\Omega\left(\varphi\frac{c_k^{n+1,*}-c_k^n}{\Delta t} - \nabla\varphi\cdot\left(\boldsymbol{u}c_k - \bar{\bar{\kappa}}\nabla c_k\right)\right)\mathrm{d}\Omega\\ &\quad+\int_{\partial\Omega}\left(\varphi\widehat{\boldsymbol{n}\cdot\boldsymbol{u}c_k} - \varphi\widehat{\boldsymbol{n}\cdot\bar{\bar{\kappa}}\nabla c_k}\right)\mathrm{d}\partial\Omega\\ &=\int_\Omega\varphi S_k\mathrm{d}\Omega,\end{aligned} \tag{4}$$

where φ is the test function in finite element methods (FEMs), the hatted term represents fluxes across the boundaries $\partial\Omega$ and $\boldsymbol{n}$ is a unit vector normal to the boundaries.

The discrete matrix form of Eq. (4) can be written as

$$\mathbf{M}\frac{\boldsymbol{c}_k^{n+1,*}-\boldsymbol{c}_k^n}{\Delta t} + \mathbf{A}(\boldsymbol{u})\boldsymbol{c}_k + \mathbf{K}\boldsymbol{c}_k = \boldsymbol{s}_k, \tag{5}$$

in which the vector $\boldsymbol{c}_k = (c_{k,1},\dots,c_{k,\mathcal{N}})^T$ contains the solution of variable c_k at nodes ($\mathcal{N}$ is the number of nodes), $\mathbf{M}$ is the mass matrix, $\mathbf{A}(\boldsymbol{u})$ is the advection operator, $\mathbf{K}$ is the diffusion operator, and $\boldsymbol{s}_k$ is the right-hand side vector containing boundary and source terms. The components of $\mathbf{M}$, $\mathbf{A}$ and $\mathbf{K}$ can be written as:

$$\begin{aligned}&\mathbf{M}_{ij} = \int_\Omega\varphi_i\varphi_j\mathrm{d}\Omega,\quad \mathbf{A}_{ij} = -\int_\Omega\nabla\varphi_i\cdot\boldsymbol{u}\varphi_j\mathrm{d}\Omega,\\ &\mathbf{K}_{ij} = \int_\Omega\nabla\varphi_i\cdot\bar{\bar{\kappa}}\nabla\varphi_j\mathrm{d}\Omega,\\ &i,j\in(1,2,\dots,\mathcal{N}).\end{aligned} \tag{6}$$

The time derivative term at time level $n+1$ is obtained using the θ-method:

$$\mathbf{M}\frac{\boldsymbol{c}_k^{n+1,*}-\boldsymbol{c}_k^n}{\Delta t} + \mathbf{A}(\boldsymbol{u}^n)\boldsymbol{c}_k^{n+\theta} + \mathbf{K}\boldsymbol{c}_k^{n+\theta} = \boldsymbol{s}_k^{n+\theta}, \tag{7}$$

where $\theta\in[0,1]$ and the terms $\boldsymbol{c}_k^{n+\theta}$ and $\boldsymbol{s}_k^{n+\theta}$ are given:

$$\boldsymbol{c}_k^{n+\theta} = \theta\boldsymbol{c}_k^{n+1,*} + (1-\theta)\boldsymbol{c}_k^n,\quad \boldsymbol{s}_k^{n+\theta} = \theta\boldsymbol{s}_k^{n+1} + (1-\theta)\boldsymbol{s}_k^n. \tag{8}$$

Eq. (7) can be rearranged for solving $\boldsymbol{c}^{n+1,*}$:

$$\left(\mathbf{M} + \theta\Delta t\left(\mathbf{A}\left(\boldsymbol{u}^n\right) + \mathbf{K}\right)\right)\boldsymbol{c}_k^{n+1,*} = \left(\mathbf{M} - (1-\theta)\Delta t\left(\mathbf{A}\left(\boldsymbol{u}^n\right) + \mathbf{K}\right)\right)\boldsymbol{c}_k^n + \boldsymbol{s}_k^{n+\theta}. \tag{9}$$

In this work, to ensure stability and suppress spurious oscillations, the control volume (CV) method is used that is handled through an alternative finite volume discretization by using a dual mesh constructed around the nodes of the parent finite element mesh. For the time discretization, the θ time stepping scheme is used to eliminate the time-step restrictions and maintain high accuracy as much as possible, where θ $(1/2 \leqslant \theta \leqslant 1)$ is chosen to be 0.5 (the Crank–Nicolson scheme) for most of the elements while large enough (close to 1) for a small fraction of individual elements with a large CFL number. In this way, the use of a large time step is acceptable when applying adaptive mesh techniques into comprehensive air quality models, which can make the computation much more efficient. For details, see Zheng et al. (2015), Pavlidis et al. (2015) and AMCG (2014). The variable c_k^{n+1} at time level $n+1$ is then updated by considering the chemical reaction in Eq. (3).

The exponential life times of the chemical species range from milliseconds to many years. The wide ranges of chemical transport and reactions pose challenges for the time integration. For computational

efficiency, the implicit and exponential time integration schemes are suggested (Zhang et al., 2011; Santillana et al., 2016; Cariolle et al., 2017). In this work, the semi-implicity time scheme is adopted for the transport solver (discussed above) while a sub-time step size adaptation strategy for the chemical kinetics solver (see Section 3.1). It is also worth noting that the exponential time integration schemes in combination to Krylov subspace methods have the potential to alleviating the restriction on the time step size from CFL or reaction rate restrictions, which allows one to use a large time step for resolving the coupled chemical transport and reaction equations, thus ensuring the computational efficiency and accuracy (Clancy and Pudykiewicz, 2013; Gaudreault and Pudykiewicz, 2016; Li et al., 2018). In exponential time integration schemes, the equations are spitted into linear and non-linear parts, where the linear part is solved analytically while the nonlinear part is computed numerically and efficiently in conjunction with Krylov subspace methods.

3. A single unified integrated photochemical model (Fluidity-Chem) with use of dynamically adaptive unstructured meshes

In this work, a new photochemical model (Fluidity-Chem) for ozone formation has been developed by incorporating a widely used chemical module CBM-Z (Zaveri and Peters, 1999) into an unstructured adaptive mesh fluid model (Fluidity) which is developed by Applied Modeling and Computation Group (AMCG) at Imperial College London (AMCG, 2014).

3.1. Photochemical mechanism

Ozone chemistry in the troposphere is driven by two major classes of precursors: volatile organic compounds ($VOCs$) and oxides of nitrogen (NO_x). It is complex and highly nonlinear with respect to the level of NO_x (Seinfeld and Pandis, 2006). There is a photochemical NO_x cycle existing between NO_x (NO and NO_2) and O_3:

$$NO_2 + h\nu \xrightarrow{O_2} NO + O_3, \quad \text{(R1)}$$

$$NO + O_3 \longrightarrow NO_2 + O_2. \quad \text{(R2)}$$

In the presence of reactive hydrocarbons(lumped as RH), the steady-state NO_x cycle will be interrupted by

$$RH + OH \xrightarrow{O_2} RO_2 + H_2O, \quad \text{(R3)}$$

$$RO_2 + NO \xrightarrow{O_2} NO_2 + R'CHO + HO_2, \quad \text{(R4)}$$

$$HO_2 + NO \longrightarrow NO_2 + OH. \quad \text{(R5)}$$

where the higher carbonyl R′CHO can, in general, continue to be oxidized. While the initiation of the hydroxyl radical OH is generated from O_3 photolysis, the propagation of OH is dominated by the conversion of NO to NO_2 by the alkyl peroxy radical RO_2 (or its corollary, the hydroperoxy radical HO_2), as shown in reactions (R3)–(R5). The main termination pathway is

$$NO_2 + OH \longrightarrow HNO_3, \quad \text{(R6)}$$

which removes both NO_2 and OH from the system. There is a competition between RH and NO_2 for the OH radical. Thus, at a high NO_x/VOC ratio (such as in a power plant plume), the reaction (R2) or (R6) will predominate, and suppress O_3 formation. As NO_x is depleted , OH reacts mainly with RH, and accelerates O_3 formation (Seinfeld and Pandis, 2006; Hamlin, 2002). This leads to the formation of ozone “wings” at the edges of plumes.

Due to thousands of species of VOCs, it is necessary to condense the hydrocarbons mechanism so that it can be used in urban and regional photochemical modeling. In the late 1980s, EPA sponsored the development of Carbon Bond Mechanism(CBM-IV) (Gery et al., 1989) that has been widely used in Lagrangian reactive plume models (e.g., RPM and SCICHEM). To better represent regional scale modeling, the modified CBM-Z version embedded in the Nested Air Quality Prediction Model System (NAQPMS) (Wang et al., 2001, 2014, 2006) has been used in this work. It contains 53 species and 132 reactions of which 45 are related to $O_3 - NO_y - HO_x$ inorganic reactions, whereas 87 are lumped organic reactions according to the types of carbon bond structure. The detailed reactions and rate coefficients are summarized in Table 2 of Zaveri and Peters (1999). For efficient and robust chemical kinetics calculation of Eq. (3), the Modified Backward Euler (MBE) solver was introduced to CBM-Z by specifying a sub-time step Δt_{sub} adaptation strategy (e.g. $5s \leqslant \Delta t_{sub} \leqslant 60s$). For details, see Feng et al. (2017).

3.2. An anisotropic unstructured mesh fluid model (Fluidity) and mesh adaptive technique

Fluidity is a computational fluid dynamics code capable of numerically solving the Navier–Stokes equation with the large eddy simulation (LES) and accompanying field equations on arbitrary unstructured meshes (AMCG, 2014; Pain et al., 2005; Zheng et al., 2015; Piggott et al., 2009, 2008a,b). The key feature of Fluidity is the use of anisotropic adaptive mesh technologies. The mesh is adapted to optimally resolve multiscale flow dynamics in fully 3D as the flow evolves.

An appropriate error measure algorithm is required to guide how the mesh is to be adapted (Pain et al., 2001). The mesh quality is gauged with respect to an error metric tensor, for example, *a-priori* or a goal based error measure (Power et al., 2006; Fang et al., 2010). The error metric is derived from the solution of variables and an error norm based on the specified interpolation error $\hat{\varepsilon}$. The error metric tensor is used for calculating the required edge length and orientation of the adapted elements. For example, for one dimensional (1D) problems, $\hat{\varepsilon} = h_e^2 |\partial^2\psi/\partial^2 x|$, where ψ is the variable solution (e.g., the species concentration) and h_e is the element length. In multi-dimensional problems, for a specified interpolation error $\hat{\varepsilon}$, the error metric is defined as follows:

$$M = \frac{1}{\hat{\varepsilon}} H = V^T \Lambda V, \quad (10)$$

where $H = \nabla^T \nabla \psi$ is the Hessian matrix for the variable ψ (here, the species concentration c_k) within an element, V is the matrix including the eigenvectors while the corresponding eigenvalues λ_i, $i \in \{1,2,3\}$ in the matrix Λ. The desired edge length h_i along the direction of the ith eigenvector of M, is calculated by $1/\sqrt{\lambda_i}$. Taking into account the maximum and minimum mesh sizes (h_{min} and h_{max}), the error metric tensor is further modified (Pain et al., 2001):

$$\tilde{M} = V^T \tilde{\Lambda} V, \quad (11)$$

in which the matrix $\tilde{\Lambda}$ includes the modified eigenvalues:

$$\tilde{\lambda}_i = \max\{\lambda_i', \frac{1}{a^2} \max_{i=1,2,3} \lambda_i'\}, \quad (12)$$

where

$$\lambda_i' = \min\left\{ \frac{1}{h_{min}^2}, \max\{|\lambda_i|, \frac{1}{h_{\max}^2}\} \right\}, \quad i \in \{1,2,3\}, \quad (13)$$

where a is the maximum aspect ratio which is introduced to bound the aspect ratio of elements in the physical space. The maximum and minimum mesh sizes are set to allow one to impose different limits in different directions.

During the mesh optimization procedure, the mesh is visited in turn and local mesh connectivity operations (edge collapsing/splitting, edge swapping, node movement, face to edge, vice versa) are performed. Numerous interpolation approaches (consistent or conservative approaches, for example) are available for projecting the variable solution from the previous mesh onto the newly adapted mesh. In this work, the consistent interpolation (interpolation by finite element basis

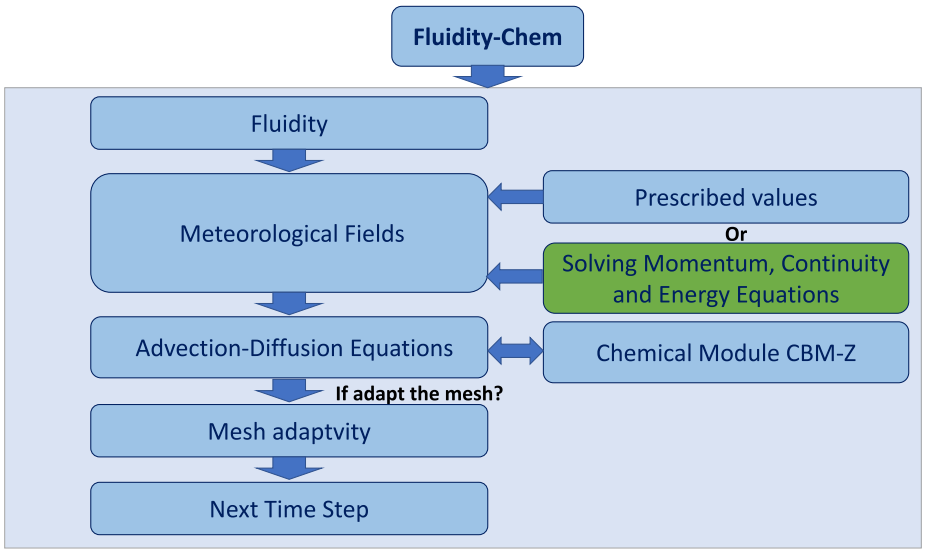

Fig. 1. Coupling of Chemical module (CBM-Z) and Fluidity with use of adaptive meshes. In this work, the meteorological fields are prescribed. The task in the green box is our future work. (For interpretation of the references to color in this figure legend, the reader is referred to the web version of this article.)

function evaluation) is adopted in mesh adaptivity (AMCG, 2014). The dynamically adaptive mesh technique ensures the computational effort to resolve important fluid dynamics at diverse scales in space and time. It is noted that the extra computational cost introduced during the adaptive mesh procedure is about ten percent of the total CPU time.

3.3. Implementation of Fluidity-Chem

The new anisotropic adaptive mesh photochemical model (Fluidity-Chem) has been implemented by integrating CBM-Z within Fluidity. The coupling of CBM-Z and Fluidity is summarized in Fig. 1. The meteorological fields can be prescribed or calculated by solving the momentum, energy and continuity equations while the spatial and temporal distribution of chemical species can be obtained by solving the convection–diffusion equation over anisotropic adaptive meshes. In this work, the meteorological fields are prescribed since the applicability of Fluidity to atmospheric flows is under development. The gas-phase chemical kinetics species are resolved at each grid node using CBM-Z. The mesh is optimally adapted with respect to the solution of selected species (here, NO and NO_2) at a regular time interval. The use of adaptive meshes enables to capture the details of small scale pollutant dispersion and chemical reactions near the point sources. The details of photochemical modeling using the adaptive mesh technique are shown in algorithm 1.

Algorithm 1: Modeling of photochemical processes

1. Initialization;
   (a) Choose the computational domain;
   (b) Set the adaptive mesh scheme
      i. Specify the error criteria for selected species;
      ii. Set the adapted time steps $t_{adapt,k}$ $(k = 1, 2, \dots)$;
      iii. Choose the minimum and maximum mesh sizes and the maximum number of nodes;
      iv. choose the aspect ratio for adapting mesh.
   (c) Initialize the wind field and provide the background of chemical species;
   (d) provide the boundary conditions;
   (e) choose numerical scheme for each variable field to be resolved.
2. Photochemical modeling using adaptive unstructured meshes (Fluidity-Chem)
   for $t_i = t_1$ *to* t_N *(here is the time loop)* **do**
      (a) Obtain/solve the wind field at current time level t_i;
      (b) Solve the advection–diffusion equation and obtain the spatial distribution of species at current time level t_i;
      (c) Solve the chemical reaction equations at each grid node:
         for $j = 1$ *to* $Nodes$ **do**
            call $CBM - Z$;
         endfor
      (d) If $t_i = t_{adapt,k}$, then adapt the mesh and interpolate the solutions from the previous mesh onto the new mesh;
   endfor
3. Output and plot the results.

4. Model performance studies

The performance of Fluidity-Chem with use of adaptive meshes has been assessed in power plant plume experiments. For comparison purpose, the meteorological and pollutant parameters were used from the plume photochemistry case in Tennessee on 12th July 1999 (Ryerson et al., 2001). The adaptive meshes were used to model the multiscale pollutant transport and chemical processes, especially the evolution and production of ozone.

4.1. Setup of model experiments

In the following numerical test cases, the computational domain is 250 km × 250 km in horizontal. A uniform vertical distribution of wind field was used in cases 1, 2 and 3 (with the assumption of fully vertical mixing, only one vertical layer is used) while the logarithmic

profile used in the vertical in case 4. At the inflow boundary, the concentration of pollutants is set to be the same as the background. The open boundary conditions (stress-free boundary conditions) are given at outflow.

The CV discretization method is used (Zheng et al., 2015). The time discretization used here is the θ time stepping scheme due to its robustness, unconditional stability and second order accuracy in time (for details, see Zheng et al. (2015) and Pavlidis et al. (2015)). The time step, dt, is set to 400 s in case studies 1, 2 and 4 while the time step is set to 20, 100 and 400 s in case study 3 (since the wind field is time dependent). To avoid the instantaneous dilution of the NO_x emissions, a high resolution mesh is provided around the plume source location. The mesh is adapted with respect to the solution of NO_x (NO and NO_2) every fourth time step. The minimum and maximum mesh sizes are set to be 100 m and 20 km respectively in horizontal while 25 m and 500 m respectively in vertical. The maximum number of nodes is set to be 10000, which is large enough to ensure the specified relative error 0.03 to be achieved. If the number of nodes required exceeds the maximum number of nodes, the error metric will be scaled, thus the actual interpolation error in the solutions will be larger than the specified one (0.03). The anisotropic gradation algorithm is used to allow for anisotropic bounds on the gradient of the mesh sizing function.

The dynamically adaptive mesh technique ensures the computational effort to resolve chemical reaction and transport processes over a wide range of spatial scales from microscale (hundred meters) to regional scale (hundred kilometers). The key issue for optimal mesh adaptivity is the selection of adapted variables, the a-priori error measure, the length of adaptive meshes and the maximum number of nodes. In the supplement document — Supporting Information, we provide further discussion and the corresponding experiments on some issues for mesh adaptivity, as well as the impact of the time stepping size and diffusion coefficient on results.

4.1.1. Case study 1: Simplified reactive plume experiment with a constant wind field

Performance of Fluidity-Chem has been first evaluated in a simplified reactive plume experiment. The assumptions in modeling setup are similar to those of Ryerson et al. (1998), where (1) the distribution of the plumes is vertically uniform within the boundary layer (1000 m), and (2) the wind speed and direction are constant (with a speed of 5 m/s). The mesh is adapted in horizontal while only one layer is set in vertical. The emission intensity of NO_x is set to be 13.9 ton/h and 1.8 ton/h (referred to Ryerson et al. (2001)). The adaptive simulation is carried out for 40,000 s (about 11 h).

Figs. 2 and 3 display the spatial distribution of the chemical species NO_x, HNO_3, O_3, HONO, PAN and HCHO at the stable stage (t = 10 hr). We can see that the high concentration of NO_x results in depletion of ozone near the plume source. It is also observed in Fig. 2 that within the distance of $x = 35 - 120$ km, the ozone enhances at the outer fringes of the plume while decreases at the plume centerline, which forms a wing-like profile of ozone across the plum section. In Fig. 3, the emission intensity (1.8 ton/h) is much smaller than that (13.9 ton/h) in Fig. 2. Due to the lower concentration of NO_x released, the formation of the ozone thus starts earlier, at the downwind distance of 20 km. The ozone is completely enhanced across the plume at x = 30 km. The wing-like structure of the ozone is seen only within the downwind distance between 20 km and 30 km.

Fig. 4 shows the net ozone production efficiency (OPE) for different NO_x emission rates from 1.8 to 13.9 ton/h, where the OPE is defined as the ratio of the integrated net ozone flux to the plant NO_x emission rate (Ryerson et al., 1998, 2001):

$$OPE = \frac{\int_S c_{o_3} \boldsymbol{u} \cdot \boldsymbol{n}_s dS}{R_{\mathrm{NO}_x}}, \tag{14}$$

in which $\boldsymbol{u}$ is the velocity vector field, S is the cross section, c_{o_3} is the concentration of net O_3, $\boldsymbol{n}_s$ is the unit vector normal to the cross section and R_{NO_x} is the emission rate of NO_x at the power plants. It is noticeable that a larger NO_X emission rate leads to a smaller OPE which is consistent with what was stated in Ryerson et al. (2001). At the downwind distance of 156 km, 5.36 molecules of ozone are produced, per molecule of NO_x released from the smallest point source (Fig. 4(d)), while 1.33 molecules of ozone are generated for the strongest point source (Fig. 4(a)). Overall, the emission intensity of NO_x strongly affects the ozone production rate over the downwind area of the power plant.

4.1.2. Case study 2: Comparison of simulated results with fixed and adaptive meshes

To demonstrate the capability of anisotropic adaptive mesh modeling, six benchmarks were carried out using the fixed and adaptive mesh schemes. The fixed mesh schemes were set up with a mesh resolution of 10 km, 5 km, 2 km and 500 m while the adaptive mesh schemes with a maximum mesh size of 20 km and a minimum mesh size of 1 km and 100 m. The corresponding results using different mesh schemes are illustrated in Figs. 5–6. It is noticed that a large numerical diffusion occurs when a coarse mesh is used. We can see that, with increasing mesh resolution, more details of structure of O_3 and NO_x can be captured. The wing-like structure of ozone is clearly seen within the downwind distance of 40–150 km of the plants with a mesh resolution of $<$ 1 km. Also it is illustrated in Figs. 5–6 that the use of a higher resolution leads to a narrower width of ozone and NO_x plumes. It is also noticeable that the grid size in adaptive mesh modeling is reduced by $>$ 95% compared to that in fixed mesh modeling while the accuracy of results remains. For example, the results using the fixed mesh resolution of 500 m is very close to that using the adaptive mesh scheme with the minimum and maximum resolution of 100 m (or 1 km) and 20 km respectively, while the number of nodes used in the fixed mesh scheme is about 50–130 times that using adaptive meshes.

4.1.3. Case study 3: Plume experiment with a wave-like wind field

The performance of the above anisotropic adaptive mesh photochemical model (Fluidity-Chem) has been further evaluated with a wave-like wind field. The setup of modeling runs is the same as case study 1 except for a wave-like wind field defined as follows:

$$u = 5 + 2\cos\frac{\pi t}{T}, \quad v = 2\cos kx + 2\cos\frac{\pi t}{T}, \tag{15}$$

where u and v are the velocity components along the x and y directions respectively, $k = 2\pi/L$, $L = 50000 \times \frac{4}{3}\, m$ and $T = 3600 \times 3\, s$.

Fig. 7 shows the spatial distribution of NO_x and O_3 at time levels t = 3 h, 6 h and 9 h. Visually the mesh is optimally adapted according to the evolving flow and pollutant features in time and space, thus providing sufficient mesh resolution where and when it is required. The fine mesh is located along the transport pathway of species during the pollutant disperse and chemical processes. Fig. 8 shows the spatial distribution of the species NO_x, HNO_3, O_3, HONO, PAN, HCHO (ppbv) at the time (t = 10 h). We can see that the use of anisotropic adaptive meshes enables to catch the details of the small scale pollutant chemical processes especially the evolution and production of ozone. The wing-like structure of ozone is clearly seen within the downwind distance of 40–100 km.

Further numerical experiments have been undertaken to estimate the effect of time step size on solutions. Fig. 9 shows the spatial distribution of NO_x and O_3 at the time t = 13 hr. We can see that the details of spatial structure of NO_x and O_3 can be represented more accurately with a smaller time step size. This suggests that a small time step size is still needed for complex meteorological fields or when there are multiple pollutant sources close to each other. The details of the impact of the time stepping size on simulational results are further discussed in the Supporting Information (see the supplement document).

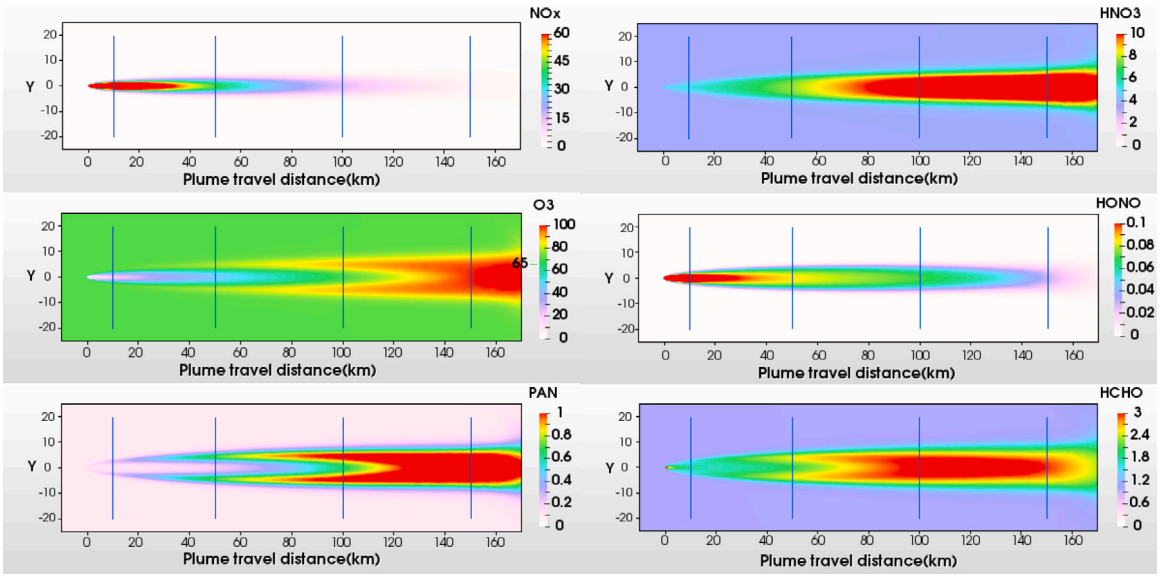

Fig. 2. Emission rate (13.9 ton/h): the spatial distribution of the species NO_x, HNO_3, O_3, HONO, PAN, HCHO (ppbv) at the stable stage (t = 10 hr), with the minimum and maximum adaptive mesh resolutions of 100 m and 20 km respectively, the time step Δt is 400 s.

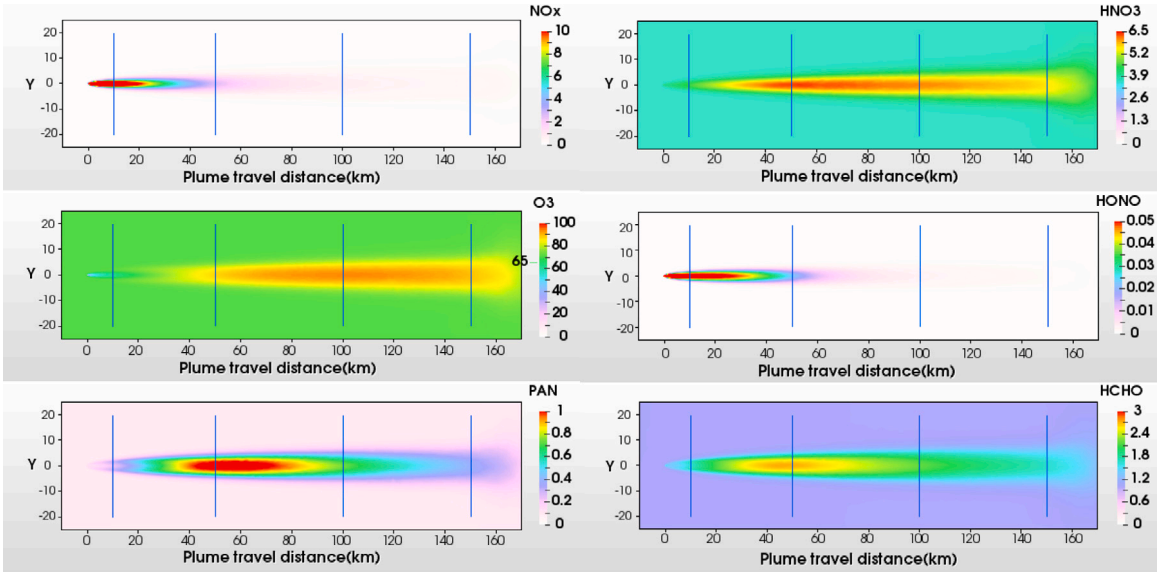

Fig. 3. Emission rate (1.8 ton/h): the spatial distribution of the species NO_x, HNO_3, O_3, HONO, PAN, HCHO (ppbv) at the stable stage (t = 10 hr), with the minimum and maximum adaptive mesh resolutions of 100 m and 20 km respectively, the time step Δt is 400 s.

4.1.4. Case study 4 (Cumberland power plant plume): Comparison between the simulated and observed concentrations of pollutants

To further evaluate the performance of adaptive meshes, Fluidity-Chem has been applied to the Cumberland power plant plume in Tennessee on 12th July 1999. The pollutant (NO_x) was continuously released from the Cumberland power plant at the emission rate of 13.9 ton/h at the height of 193.5 m. The comparison between the model results and SOS 1999 aircraft plume data was carried out. During the SOS 1999 campaign, NOAA WP-3D aircraft was flown pass upwind and downwind of the Cumberland power plant, measuring the mixing ratios of atmospheric species. The design of the flight track (see Figure S11 in the Supporting Information) ensured that the distribution of plumes was well measured (Ryerson et al., 2001).

In 3D modeling set up, a logarithmic vertical profile of wind field is used within the boundary layer (2000 m) where an average wind speed is 5 m/s and the wind direction is almost constant from the north. Based on the BEIS-2 isoprene emission estimate for the month of July, the Isoprene Flux is set to be $6.0 * 10^{15}$ mol/m^2/s (Stroud et al., 2001). A constant turbulent diffusivity is set to 200 m^2/s in horizontal and 10 m^2/s in vertical for all species. The details of the impact of the turbulent diffusivity on simulated results are discussed in the Supporting Information. The simulation period is 0:00–18:00 on 12, July 1999. The adaptive meshes are used to model the multiscale pollutant transport and chemical processes, especially the evolution and production of ozone. The minimum and maximum mesh sizes are set to 100 m and 20 km respectively in horizontal while 25 m and 500 m respectively in vertical. The initial mesh and the adaptive mesh at t = 12 h are shown in Figure S10 and Fig. 10 respectively.

Figs. 11 and 12 show the simulated and observed pollutants (NO_x and O_3) at different downwind distances of the Cumberland power plant. Within 66 km downwind distance, the model predicts the slender high NO_x plumes within several kilometers width where the relative error in the peak value of NO_x and O_3 is between 10%–20% (see Fig. 11). With the use of adaptive meshes, there is an improvement in modeling

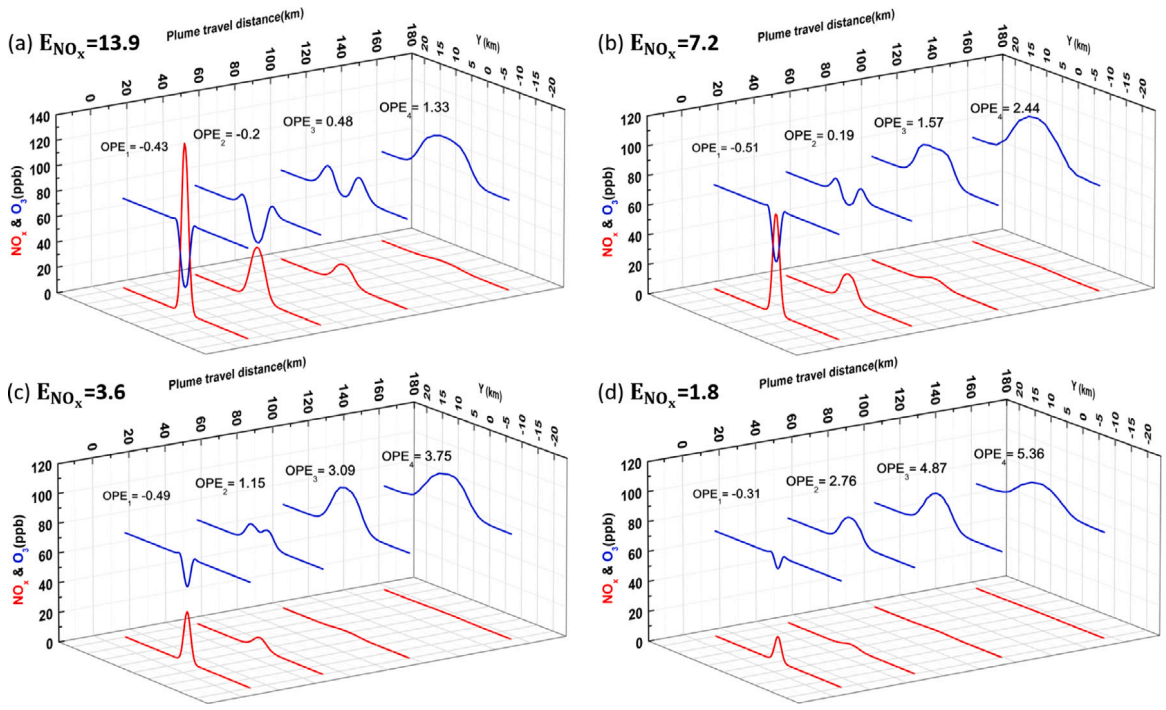

Fig. 4. Net ozone production efficiency (OPE) with different NO_x emission rates.

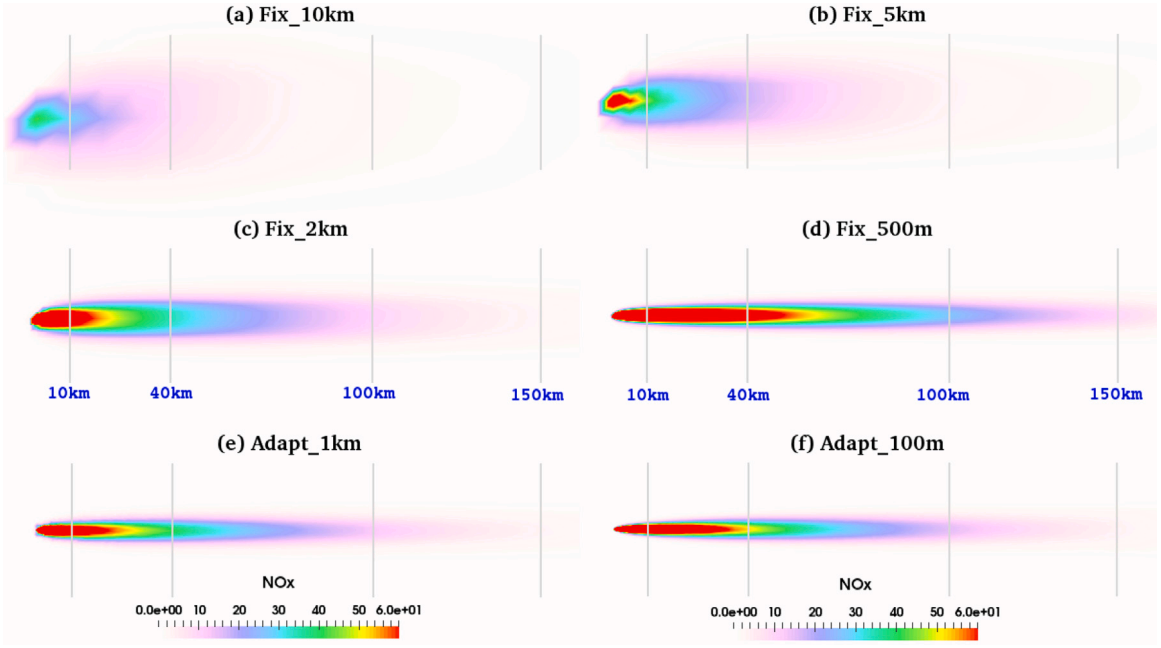

Fig. 5. Comparison of NO_x distribution using fixed meshes with a resolution of (a) 10 km (676 nodes used); (b) 5 km (2601 nodes used); (c) 2 km (15876 nodes used); (d) 500 *m* (251001 nodes used); and adaptive meshes with a maximum resolution of 20 km and a minimum resolution of (e) 1 km (1855 nodes used) and (f) 100 m (5046 nodes used).

accuracy, especially the representation of the wing-like structure of O_3 concentration in comparison to the published results in Chowdhury et al. (2015). Further downwind distance of 66–156 km, there is a good correlation between the observed data and simulated results although some difference in the peak is noticeable. The discrepancy between the observed and simulated results may be caused by the ideal wind field, constant diffusivity and flat terrain assumed in the simulation. This can be improved by coupling the model with WRF model or atmospheric model in Fluidity when it is developed in future, where the eddy mixing can be well represented.

The simulated results illustrate that after NO_x is released from the point source the evolution of O_3 can be divided into three stages: the initial stage (with a dominant NO_x and ozone titration) within the distance of 50 km from the point source; the plume growth stage (where O_3 formation starts at the outer fringes of the plume) with the distance of 50–100 km and the mature plume stage (ozone enhancement across the plume) within the distance of > 100 km. Ryerson et al. (2001) pointed out that ozone concentration is enhanced when NO_x < 10 ppbv while ozone is suppressed at NO_x > 15 ppbv. This is also approved by both the observed and simulated results in this case (see Figs. 2, 11 and 12). At the initial stage (with the distance of < 50 km), a high

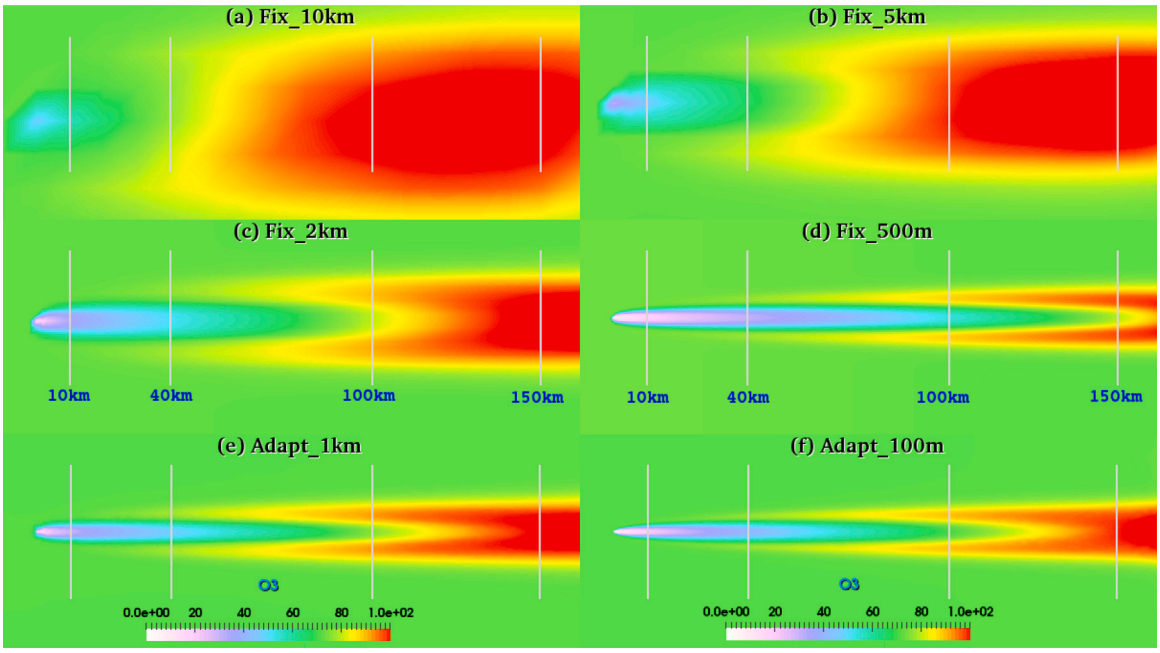

Fig. 6. Comparison of O_3 distribution using different resolution mesh, same as Fig. 5.

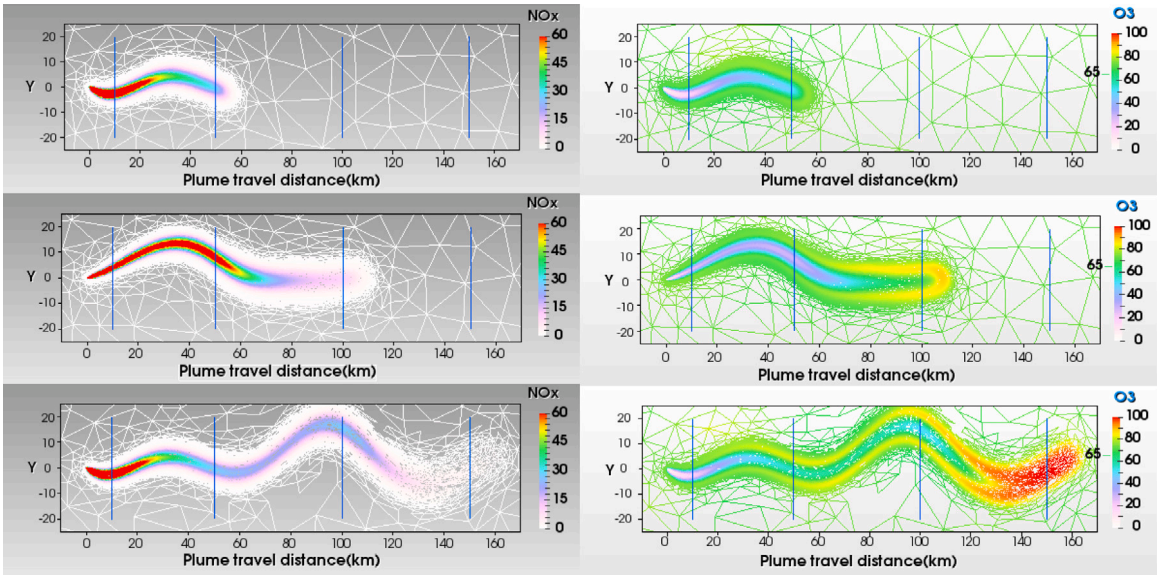

Fig. 7. Emission rate (13.9 ton/h) with a wave-like wind field: the spatial distribution of O_3 (left) and NO_x (right) at time levels t = 3 hr, 6 h and 9 h where an adaptive mesh scheme is used with the minimum and maximum resolutions of 100 m and 20 km respectively, the time step Δt is 20 s.

concentration of NO_x (between 50–150 ppbv) in the center of the plume leads to a depletion of ozone. At the growth stage (50–100 km), the formation of ozone begins at the outer fringes of the plume (within the crosswind distance of 3–8 km from the center, where the concentration of NO_x is less than 10 ppbv), while the ozone is still depleted at the center of the plume. We can see that the wing-like structure of ozone can be resolved with adaptive meshes.

In most of existing air quality models, it is difficult to simulate the details of the wing-like structure of ozone over a long distance due to the limitation of mesh resolutions in simulations especially for a large plume emission (Chowdhury et al., 2015). A coarse mesh resolution leads to the dilution of NO_x across a mesh. Therefore, the wing-like structure of O_3 concentration at the plume growth stage cannot usually be seen in numerical simulations if the resolution of meshes is not high enough. In the past years, a number of approaches have been developed to tackle this challenge, for example, nested/adapted grids, hybrids modeling and an embedded sub-grid scale plume model (PinG) (Karamchandani et al., 2011; Srivastava et al., 2001). Among these approaches, the use of adaptive meshes is the effective and efficient one that can simulate simultaneously the puff transport and chemical processes over a range of scales from meters to tons of kilometers without the Gaussian distribution assumption (often used in most of existing modules, e.g. PinG). It is illustrated in our test cases that the adaptive unstructured mesh model can capture the details of the wing-like structure of ozone concentration in both small and large plume emissions.

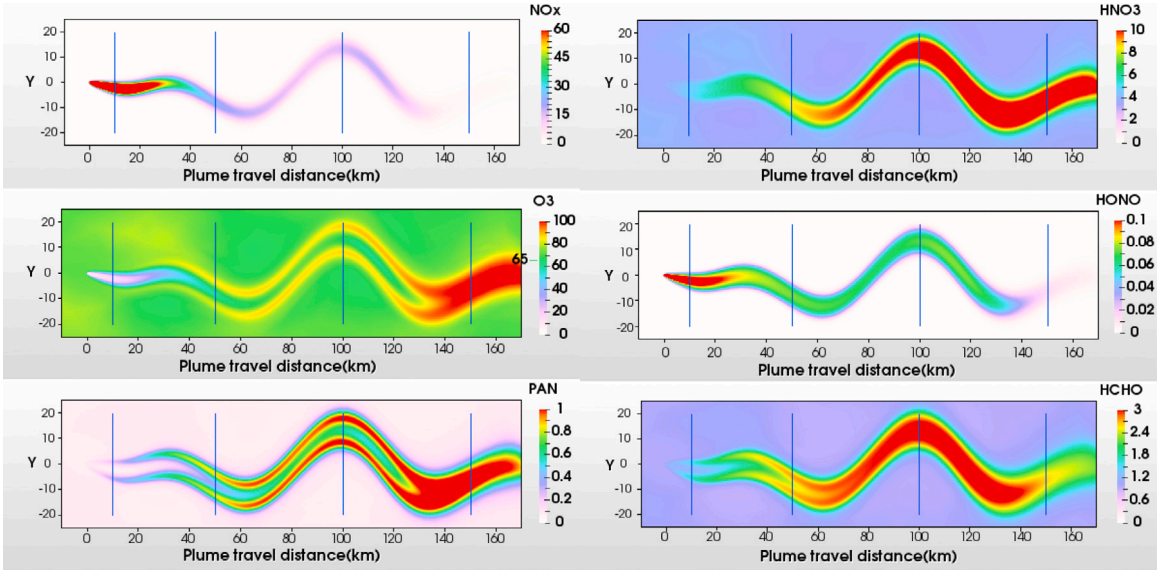

Fig. 8. Emission rate (13.9 ton/h) with a wave-like wind field: the spatial distribution of the species NO_x, HNO_3, O_3, HONO, PAN, HCHO (ppbv) at time t = 10 hr, with the minimum and maximum adaptive mesh resolutions of 100 m and 20 km respectively, the time step Δt is 20 s.

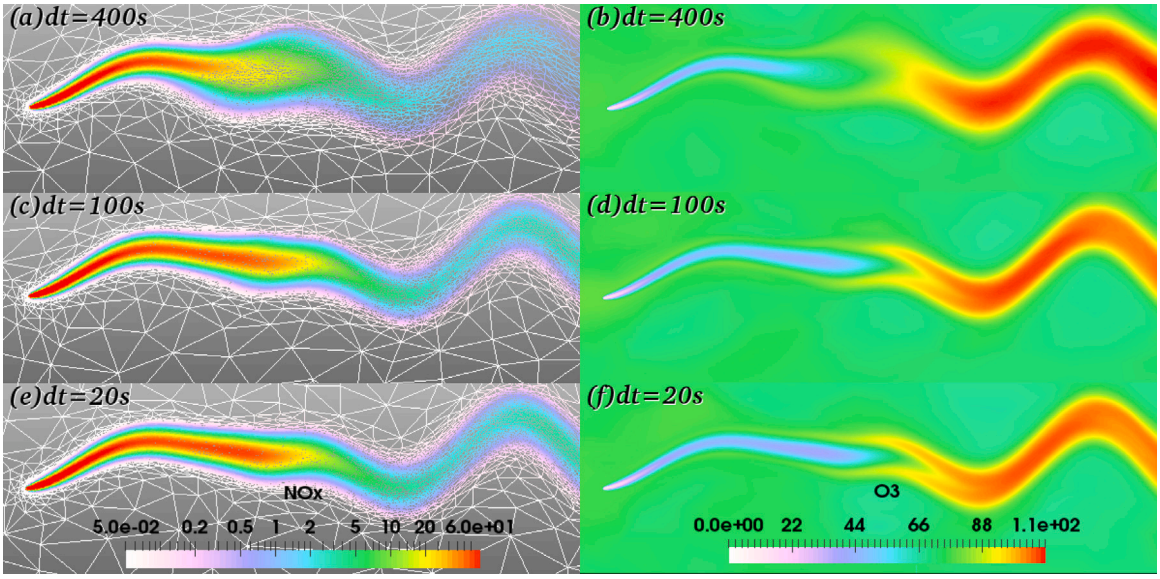

Fig. 9. Emission rate (13.9 ton/h) with a wave-like wind field: the spatial distribution of the species NO_x and O_3 at time t = 13 hr, with different time step sizes of 400 s, 100 s and 20 s.

5. Conclusions

This article has presented a newly developed photochemical transport model (Fluidity-Chem) for use in simulating the complex dispersion and chemical process after plumes are released from power plants. An adaptive anisotropic unstructured mesh technique has been introduced to chemical modeling. The mesh is optimally adapted in time and space in response to the evolving flow and chemical features. Over most of photochemical models, the use of dynamically adaptive anisotropic meshes enables us to resolve the plume dynamic and chemical processes (plume initialization, growth and mature stages) from a small scale (meters, near the point sources) up to a large scale (tons of kilometers) simultaneously. Evaluation of Fluidity-Chem performance has been carried out by comparing the simulated results against the measurements during the plume dispersion and photochemical processes. The adaptive mesh can capture the details of the plume chemical evolution: the slender high-NO_x puff structure at initial stage and the wing-like O_3 structure at the growth stage. Further evaluation of Fluidity-Chem has been tested with a wave-like wind field. It is noted that the Fluidity-Chem is not coupled with the atmospherical model within Fluidity since the applicability of Fluidity for atmospheric flows is still under development. This will be our focus in future work. First, the dynamically adaptive mesh photochemical model will be coupled with existing dynamic fluid flow models (e.g. the Weather Research and Forecast — WRF model) for resolving the meteorological fields in realistic cases. The consistent interpolation method used in Zheng et al. (2015) will be introduced to bridge the unstructured meshes in Fluidity and structured meshes in WRF. Furthermore, the adaptive mesh photochemical model developed here will finally be coupled with the atmospheric model in Fluidity when it is ready.

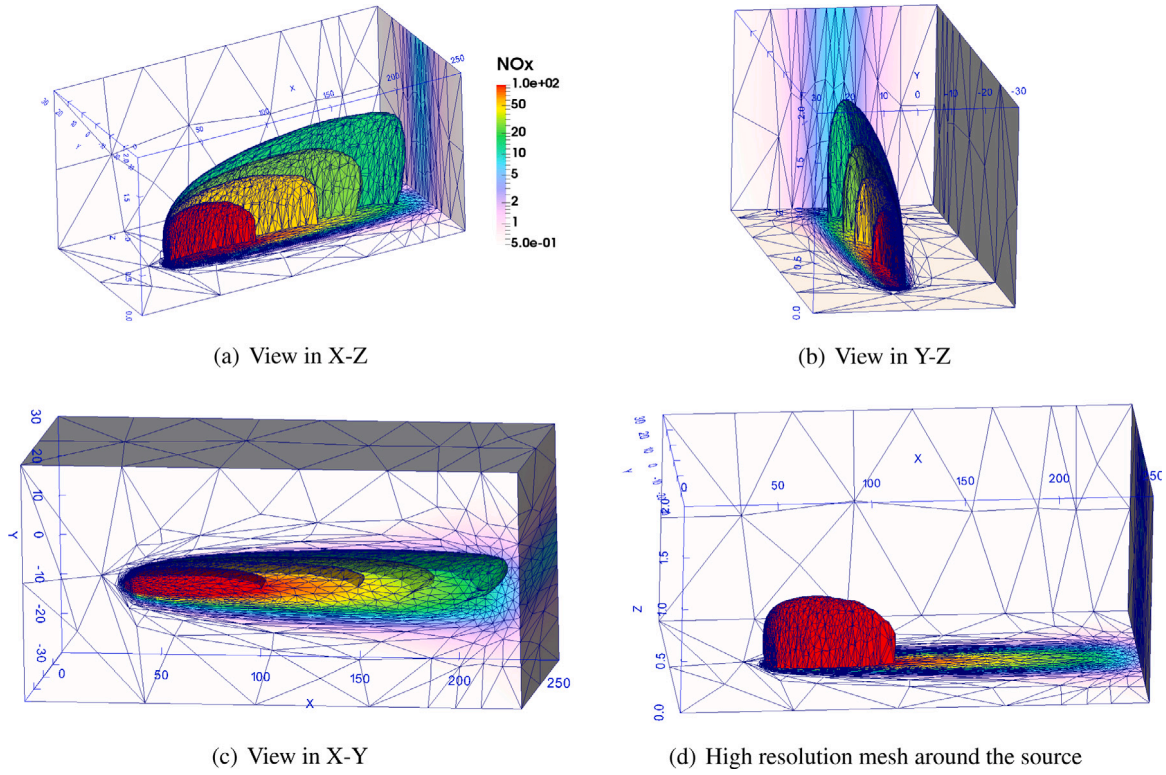

(a) View in X-Z (b) View in Y-Z

(c) View in X-Y (d) High resolution mesh around the source

Fig. 10. Case study 4 — Cumberland power plant plume at time $t = 12$ h: the different views of 3D plume visualization, surface NO_x concentration(ppbv) and the corresponding adaptive mesh.

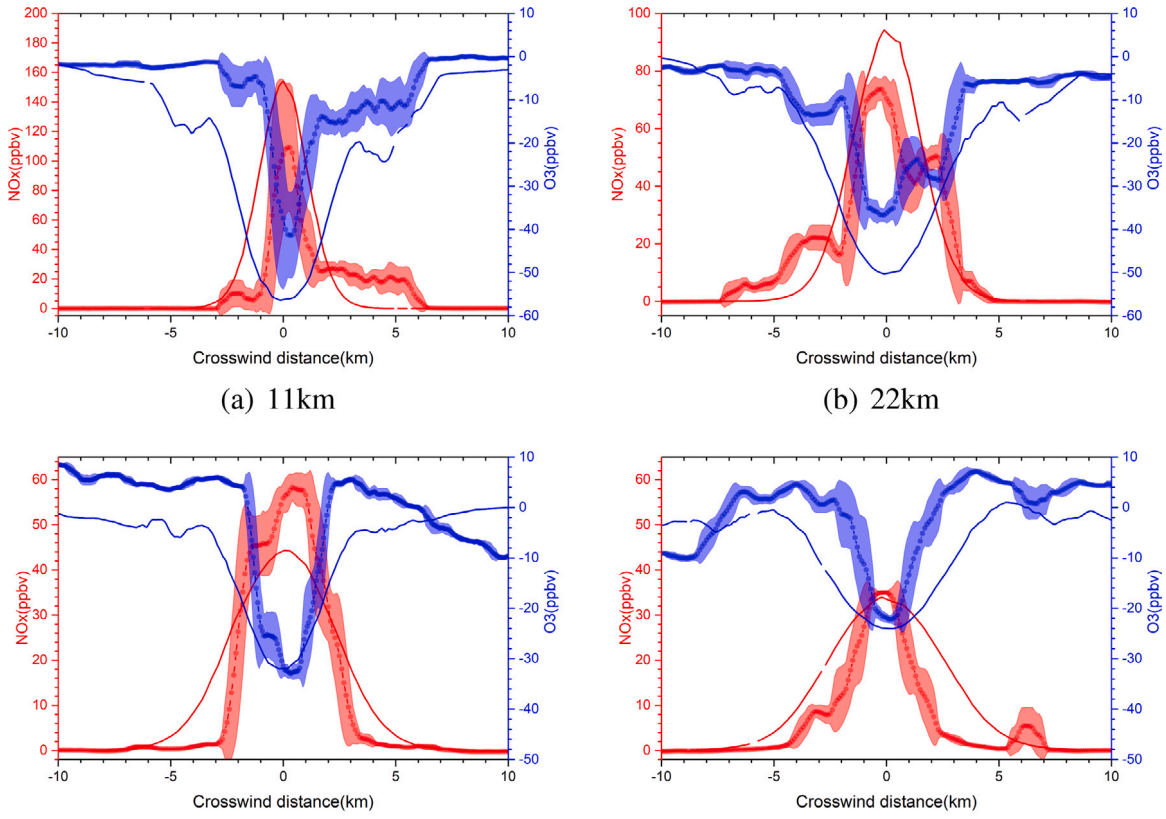

(a) 11km (b) 22km

(c) 51km (d) 66km

Fig. 11. Comparison of the observed (dash-dotted line with a shade area) and simulated (solid line) perturbation NO_x and O_3 (ppbv) for Cumberland plume traverse study at the downwind distance of 11, 22, 51, 66 km. The observed data are represented as 11-s running average of 1-s values while the shade area represents one standard deviation from the average value.

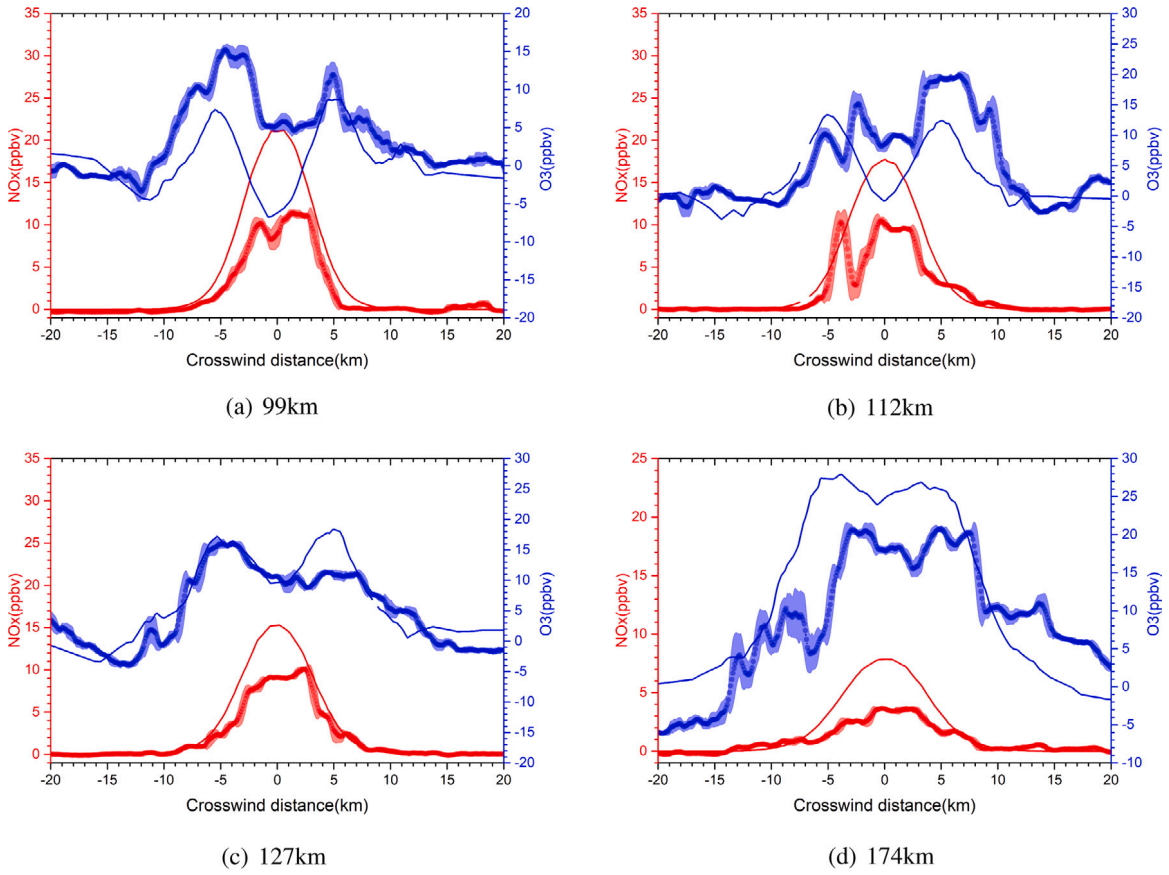

Fig. 12. Same as in Fig. 11 except for at the downwind distance of 99, 112, 127, 174 km. Comparison of the simulated results for different turbulent diffusivity $K = 100, 200$ and 300 m^2/s is shown in Figure S9 in the Supporting Information.

Declaration of competing interest

The authors declare that they have no known competing financial interests or personal relationships that could have appeared to influence the work reported in this paper.

CRediT authorship contribution statement

J. Zheng: Software, Writing - original draft, Methodology, Validation, Investigation. **F. Fang:** Supervision, Writing - review & editing, Conceptualization, Software, Methodology. **Z. Wang:** Visualization, Software. **J. Zhu:** Visualization, Conceptualization. **J. Li:** Formal analysis. **J. Li:** Visualization. **H. Xiao:** Resources. **C.C. Pain:** Methodology.

Acknowledgments

The authors are grateful for the support of the National Key Research and Development Program of China (grant no: 2017YFC0209800), the UK's the Engineering and Physical Sciences Research Council fund for Managing air for greener inner cities (MAGIC) (EP/N010221/1) and INHALE, China (EP/T003189/1), the Royal Society (IEC/NS- C/170563) in the UK, the National Natural Science Foundation of China (grant no: 41705104), and Ningbo Science and Technology Plan Project in China [http://dx.doi.org/10.13039/501100007928] (2017C50004). The authors thanks to Dr F. Feng for helpful discussions. We thank the NOAA Aircraft Operations Center for use of the SOS 1999 observational data. Finally, we would like to thank the two reviewers for their in-depth comments that contributed to improving the presentation of our paper.

Appendix A. Supplementary data - Other key issues for mesh adaptivity and numerical schemes in simulations

Supplementary material related to this article can be found online at https://doi.org/10.1016/j.atmosenv.2020.117431.

References

AMCG, 2014. Fluidity Manual. Applied Modelling and Computation Group, Imperial College London, URL http://fluidityproject.github.io/support.html.

Arunachalam, S., Holland, A., Do, B., Abraczinskas, M., 2006. A quantitative assessment of the influence of grid resolution on predictions of future-year air quality in north Carolina, USA. Atmos. Environ. 40 (26), 5010–5026.

Baker, C., Buchan, A., Pain, C., Farrell, P., Eaton, M., Warner, P., 2013. Multimesh anisotropic adaptivity for the Boltzmann transport equation. Ann. Nucl. Energy 53, 411–426.

Behrens, J., 2006. Adaptive atmospheric modeling: Key techniques in grid generation, data structures, and numerical operations with applications. Lect. Notes Comput. Sci. Eng.

Cariolle, D., Moinat, P., Teyssèdre, H., Giraud, L., Josse, B., Lefèvre, F., 2017. ASIS V1.0: an adaptive solver for the simulation of atmospheric chemistry. Geosci. Model Dev. 10, 1467–1485.

Chowdhury, B., Karamchandani, P.K., Sykes, R.I., Henn, D.S., Knipping, E., 2015. Reactive puff model SCICHEM: Model enhancements and performance studies. Atmos. Environ. 117, 242–258. http://dx.doi.org/10.1016/j.atmosenv.2015.07.012.

Clancy, C., Pudykiewicz, J.A., 2013. On the use of exponential time integration methods in atmospheric models. Tellus A 65 (1), 20898.

Constantinescu, E.M., Sandu, A., Carmichael, G.R., 2008. Modeling atmospheric chemistry and transport with dynamic adaptive resolution. Comput. Geosci. 12 (2), 133–151.

Dietachmayer, G.S., Droegemeier, K.K., 1992. Application of continuous dynamic grid adaption techniques to meteorological modeling. Part I: Basic formulation and accuracy. Mon. Weather Rev. 120 (8), 1675–1706.

Fang, F., Pain, C., Navon, I., Gorman, G., Piggott, M., Allison, P., Goddard, A., 2010. A POD goal-oriented error measure for mesh optimization. Internat. J. Numer. Methods Fluids 63 (2), 185–206.

Feng, F., Chi, X., Wang, Z., Li, J., Jiang, J., Yang, W., 2017. A nonnegativity preserved efficient chemical solver applied to the air pollution forecast. Appl. Math. Comput. 314, 44–57.

Garcia-Menendez, F., Odman, M.T., 2011. Adaptive grid use in air quality modeling. Atmosphere 2 (3), 484–509.

Garcia-Menendez, F., Yano, A., Hu, Y., Odman, M.T., 2010. An adaptive grid version of CMAQ for improving the resolution of plumes. Atmospheric Pollut. Res. 1 (4), 239–249.

Gaudreault, S., Pudykiewicz, J.A., 2016. An efficient exponential time integration method for the numerical solution of the shallow water equations on the sphere. J. Comput. Phys. 322, 827–848.

Gery, M.W., Whitten, G.Z., Killus, J.P., Dodge, M.C., 1989. A photochemical kinetics mechanism for urban and regional scale computer modeling. J. Geophys. Res.: Atmos. 94 (D10), 12925–12956.

Hamlin, D.T., 2002. Modeling Ozone Formation in a Central Texas Power Plant Plume (Ph.D. thesis). University of Texas at Austin.

Karamchandani, P., Santos, L., Sykes, I., Zhang, Y., Tonne, C., Seigneur, C., 2000. Development and evaluation of a state-of-the-science reactive plume model. Environ. Sci. Technol. 34 (5), 870–880.

Karamchandani, P., Vijayaraghavan, K., Yarwood, G., 2011. Sub-grid scale plume modeling. Atmosphere 2 (4), 389–406.

Karamchandani, P., Zhang, Y., Chen, S.-Y., 2012. Development and initial application of a sub-grid scale plume treatment in a state-of-the-art online multi-scale air quality and weather prediction model. Atmos. Environ. 63, 125–134.

Kim, Y.H., Kim, H.S., Song, C.H., 2017. Development of a reactive plume model for the consideration of power-plant plume photochemistry and its applications. Environ. Sci. Technol. 51 (3), 1477–1487. http://dx.doi.org/10.1021/acs.est.6b03919, https://www.ncbi.nlm.nih.gov/pubmed/28068079.

Kühnlein, C., 2011. Solution-Adaptive Moving Mesh Solver for Geophysical Flows (Ph.D. thesis). lmu.

Kühnlein, C., Smolarkiewicz, P.K., Dörnbrack, A., 2012. Modelling atmospheric flows with adaptive moving meshes. J. Comput. Phys. 231 (7), 2741–2763.

Lagzi, I., Turányi, T., Tomlin, A.S., Haszpra, L., 2009. Modelling photochemical air pollutant formation in Hungary using an adaptive grid technique. Int. J. Environ. Pollut. 36 (1), 44–58.

Li, S.-J., Luo, L.-S., Wang, Z.J., Ju, L., 2018. An exponential time-integrator scheme for steady and unsteady inviscid flows. J. Comput. Phys. 365, 206–225.

Mauzerall, D., Sultan, B., Kim, N., Bradford, D., 2005. NO Emissions from large point sources: variability in ozone production, resulting health damages and economic costs. Atmos. Environ. 39 (16), 2851–2866. http://dx.doi.org/10.1016/j.atmosenv.2004.12.041.

Nikiforakis, N., 2009. Mesh generation and mesh adaptation for large-scale earth-system modelling. Phil. Trans. R. Soc. A 367 (1907), 4473–4481.

Odman, M.T., Khan, M., 2002. Adaptive grid air quality model: Application to an ozone episode. In: Proceedings of the 12th Joint Conference on the Applications of Air Pollution Meteorology with the Air and Waste Management Association, Norfolk, VA, USA.

Odman, M.T., Khan, M., Srivastava, R., McRae, D.S., 2004. Initial application of the adaptive grid air quality model. In: Air Pollution Modeling and Its Application XV. Springer, pp. 319–328.

Pain, C., Piggott, M., Goddard, A., Fang, F., Gorman, G., Marshall, D., Eaton, M., Power, P., De Oliveira, C., 2005. Three-dimensional unstructured mesh ocean modelling. Ocean Model. 10 (1), 5–33.

Pain, C., Umpleby, A., De Oliveira, C., Goddard, A., 2001. Tetrahedral mesh optimisation and adaptivity for steady-state and transient finite element calculations. Comput. Methods Appl. Mech. Engrg. 190 (29), 3771–3796.

Pavlidis, D., Gomes, J.L., Xie, Z., Percival, J.R., Pain, C.C., Matar, O.K., 2015. Compressive advection and multi-component methods for interface-capturing. Internat. J. Numer. Methods Fluids 80 (4), 256–282.

Piggott, M., Farrell, P., Wilson, C., Gorman, G., Pain, C., 2009. Anisotropic mesh adaptivity for multi-scale ocean modelling. Phil. Trans. R. Soc. A 367 (1907), 4591–4611.

Piggott, M., Gorman, G., Pain, C., Allison, P., Candy, A., Martin, B., Wells, M., 2008a. A new computational framework for multi-scale ocean modelling based on adapting unstructured meshes. Internat. J. Numer. Methods Fluids 56 (8), 1003–1015.

Piggott, M.D., Pain, C.C., Gorman, G.J., Marshall, D.P., Killworth, P.D., 2008b. Unstructured adaptive meshes for ocean modeling. Geophys. Monogr. Ser. 177, 383–408.

Piggott, M., Pain, C., Gorman, G., Power, P., Goddard, A., 2005. h, r, and hr adaptivity with applications in numerical ocean modelling. Ocean Model. 10 (1), 95–113.

Power, P., Pain, C.C., Piggott, M., Fang, F., Gorman, G.J., Umpleby, A., Goddard, A.J., Navon, I., 2006. Adjoint a posteriori error measures for anisotropic mesh optimisation. Comput. Math. Appl. 52 (8–9), 1213–1242.

Queen, A., Zhang, Y., 2008. Examining the sensitivity of mm5–CMAQ predictions to explicit microphysics schemes and horizontal grid resolutions, Part III–The impact of horizontal grid resolution. Atmos. Environ. 42 (16), 3869–3881.

Ryerson, T.B., Buhr, M.P., Frost, G.J., Goldan, P.D., Holloway, J.S., Hübler, G., Jobson, B.T., Kuster, W.C., McKeen, S.A., Parrish, D.D., Roberts, J.M., Sueper, D.T., Trainer, M., Williams, J., Fehsenfeld, F.C., 1998. Emissions lifetimes and ozone formation in power plant plumes. J. Geophys. Res.: Atmos. 103 (D17), 22569–22583. http://dx.doi.org/10.1029/98jd01620.

Ryerson, T.B., Trainer, M., Holloway, J.S., Parrish, D.D., Huey, L.G., Sueper, D.T., Frost, G.J., Donnelly, S.G., Schauffler, S., Atlas, E.L., Kuster, W.C., Goldan, P.D., Hubler, G., Meagher, J.F., Fehsenfeld, F.C., 2001. Observations of ozone formation in power plant plumes and implications for ozone control strategies. Science 292 (5517), 719–723. http://dx.doi.org/10.1126/science.1058113, https://www.ncbi.nlm.nih.gov/pubmed/11326097.

Santillana, M., Zhang, L., Yantosca, R., 2016. Estimating numerical errors due to operator splitting in global atmospheric chemistry models: Transport and chemistry. J. Comput. Phys. 305, 372–386.

Seinfeld, J.H., Pandis, S.N., 2006. Atmospheric Chemistry and Physics: from Air Pollution to Climate Change. John Willey & Sons, Inc., New York.

Srivastava, R.K., McRae, D., Odman, M., 2000. An adaptive grid algorithm for air-quality modeling. J. Comput. Phys. 165 (2), 437–472.

Srivastava, R., McRae, D., Odman, M., 2001. Simulation of dispersion of a power plant plume using an adaptive grid algorithm. Atmos. Environ. 35 (28), 4801–4818.

Stroud, C.A., Roberts, J.M., Goldan, P.D., Kuster, W.C., Murphy, P.C., Williams, E.J., Hereid, D., Parrish, D., Sueper, D., Trainer, M., Fehsenfeld, F.C., Apel, E.C., Riemer, D., Wert, B., Henry, B., Fried, A., Martinez-Harder, M., Harder, H., Brune, W.H., Li, G., Xie, H., Young, V.L., 2001. Isoprene and its oxidation products, methacrolein and methylvinyl ketone, at an urban forested site during the 1999 southern oxidants study. J. Geophys. Res.: Atmos. 106 (D8), 8035–8046. http://dx.doi.org/10.1029/2000JD900628, https://agupubs.onlinelibrary.wiley.com/doi/abs/10.1029/2000JD900628.

Taghavi, M., Cautenet, S., Foret, G., 2004. Simulation of ozone production in a complex circulation region using nested grids. Atmos. Chem. Phys. 4 (3), 825–838.

Wang, Z., Li, J., Wang, X., Pochanart, P., Akimoto, H., 2006. Modeling of regional high ozone episode observed at two mountain sites (Mt. Tai and Huang) in East China. J. Atmos. Chem. 55 (3), 253–272.

Wang, Z., Li, J., et al., 2014. Modeling study of regional severe hazes over mid-eastern China in January 2013 and its implications on pollution prevention and control. Sci. China Earth Sci. 57 (1), 3–13.

Wang, Z., Maeda, T., Hayashi, M., Hsiao, L.-F., Liu, K.-Y., 2001. A nested air quality prediction modeling system for urban and regional scales: Application for high-ozone episode in Taiwan. Water, Air, Soil Pollut. 130 (1–4), 391–396.

Weller, H., Ringler, T., Piggott, M., Wood, N., 2010. Challenges facing adaptive mesh modeling of the atmosphere and ocean. Bull. Am. Meteorol. Soc. 91 (1), 105–108.

Zaveri, R.A., Peters, L.K., 1999. A new lumped structure photochemical mechanism for large-scale applications. J. Geophys. Res.: Atmos. 104 (D23), 30387–30415. http://dx.doi.org/10.1029/1999jd900876.

Zhang, H., Linford, J.C., Sandu, A., Sander, R., 2011. Chemical mechanism solvers in air quality models. Atmosphere 2 (3), 510–532.

Zheng, J., Zhu, J., Wang, Z., Fang, F., Pain, C.C., Xiang, J., 2015. Towards a new multiscale air quality transport model using the fully unstructured anisotropic adaptive mesh technology of fluidity (version 4.1.9). Geosci. Model Dev. 8 (10), 3421–3440, https://www.geosci-model-dev.net/8/3421/2015/.